

Single-Ion Spectroscopy of h-BN Point Defect Fluorescence in Liquid Environments

Yecun Wu¹, Kun Xu², Hori Pada Sarker³, Takashi Taniguchi⁴, Kenji Watanabe⁴, Frank Abild-Pedersen³, Arun Majumdar^{2,5}, Yi Cui^{5,6,7}, Yan-Kai Tzeng⁸, Steven Chu^{1,5,9}

1. Department of Physics, Stanford University, Stanford, CA, USA
2. Department of Mechanical Engineering, Stanford University, Stanford, CA, USA
3. SUNCAT Center for Interface Science and Catalysis, SLAC National Accelerator Laboratory, 2575 Sand Hill Road, Menlo Park, CA, USA.
4. International Center for Materials Nanoarchitectonics, National Institute for Materials Science, Tsukuba, Japan
5. Department of Energy Science and Engineering, Stanford University, Stanford, CA, USA
6. Department of Materials Science and Engineering, Stanford University, Stanford, CA, USA
7. Stanford Institute for Materials and Energy Sciences, SLAC National Accelerator Laboratory, 2575 Sand Hill Road, Menlo Park, CA, USA.
8. Applied Energy Division, SLAC National Accelerator Laboratory, 2575 Sand Hill Road, Menlo Park, CA, USA.
9. Department of Molecular and Cellular Physiology, Stanford University, Stanford, CA, USA

Corresponding authors:

Yan-Kai Tzeng (ytzeng@slac.stanford.edu), Steven Chu (schu@stanford.edu)

Abstract

Understanding individual ions in solutions is essential for advancing our knowledge of complex chemical systems. However, tracking and detecting ions at the single-ion level in liquid environments remains a challenge. We introduce a strategy for visualization and differentiation of different ions in liquid environment via point defects in hexagonal boron nitride (h-BN) as the ion sensor. Ions interacting with the optically active point defects in h-BN alter emission properties, allowing us to capture these changes and visualize single ions. Using Li^+ in organic electrolytes as a model, we observed a spectral shift of over 10 nm upon Li^+ addition, and an over 50 nm red shift with applied electric fields due to reactions between Li^+ and h-BN point defects. Frequency domain analysis further revealed the rapid dynamics of ion migration and the slow electrochemical reactions. We further spectroscopically differentiated various ions (H^+ , Li^+ , Na^+ , K^+ , Zn^{2+} , Al^{3+}) in aqueous solution. Each ion, with its distinct electron cloud configuration, interacts distinctively with the electron clouds of h-BN defects, resulting in specific and identifiable spectroscopic signatures. This ion sensing platform enables the direct visualization and differentiation of individual ions in a liquid environment, offering insights into chemical reactions at the single-ion level. This capability presents potential applications in various fields involving ions in liquids, including but not limited to biology, battery technology, and environmental science.

Introduction

The ability to precisely detect and differentiate different ions in the same solution or the same ion in different solutions is critical across a wide range of scientific and technological fields. In biological systems, maintaining ion homeostasis is essential for cellular function, signaling, and overall organism health.^{1,2} Environmental monitoring relies on accurate ion detection to assess and mitigate pollution, ensuring the safety of water sources and protecting ecosystems.³ In industrial processes, such as chemical manufacturing and metal extraction,⁴ ion differentiation is crucial for optimizing performance and ensuring safety.

Traditional methods for ion detection include ion chromatography,⁵ mass spectrometry,⁶⁻⁸ and electrochemical sensors.⁹⁻¹¹ These methods offer high sensitivity and accuracy but often involve complex, time-consuming procedures and sophisticated instrumentation. Additionally, none of these existing methods provide real-time information down to a single ion limit. In addition, the development of fluorescent and chromogenic dyes allows the detection of heavy metal ions through optical methods.^{12,13} However, the optical detection of light ions such as H^+ and Li^+ remains challenging due to their lower electron densities and lack of specific binding sites in dyes.

Given these limitations, there is a pressing need for innovative approaches that can provide rapid, sensitive, and selective ion detection in diverse liquid environments without disturbing the systems of interest. This is where advancements in materials science, particularly the use of h-BN with optically active point defects, present a promising alternative. The single point defect in h-BN has been demonstrated to be optically active as a quantum emitter.¹⁴⁻¹⁷ These quantum emitters are sensitive to changes in their surrounding environment and exhibit activity in the presence of protons and specific organic solvents.^{18,19} Using single molecule localization microscopy (SMLM),²⁰⁻²³ the trajectories of protons or organic molecules can be extracted, enhancing our understanding of their dynamics. Nevertheless, the spectral information, which reflects the local electronic structure associated with the defects and indicates the chemical behavior of the surrounding environment, remains unexplored.

We first studied Li^+ interactions with point defects in h-BN in various electrolytes. By utilizing SMLM combined with a multispectral localization technique, we observed a red shift in the emission wavelength exceeding 10 nm upon adding Li^+ to the electrolytes. This shift is attributed to the occupancy of lithium ions at the defect sites across three different electrolytes. Subsequently, we applied voltages to induce electrochemical reactions between the point defects and Li^+ . When Li^+ was driven onto the point defects in h-BN surface, a more pronounced red shift of over 50 nm in the spectra was detected, suggesting a de-solvation and insertion process. Frequency domain analysis highlighted the differing dynamics between ion migration and electrochemical reactions.

We then expanded our investigations to include multiple ions, such as H^+ , Na^+ , K^+ , Zn^{2+} , and Al^{3+} . Each ion, with its unique electron cloud configuration, interacted distinctively with the

electron clouds of h-BN defects. These interactions resulted in variations in the spectral information emitted by the point defects in h-BN. Leveraging these spectral differences enables accurate distinction between different ion types in a solution. This capability allows for precise identification and tracking of individual ions, offering deeper insights into their behavior and interactions at a single-ion scale.

Ultimately, our results offer a strategy to detect and visualize ions in liquid at the single-ion limit. This work has the potential to significantly benefit various fields that involve ions in liquid environments. In the study of energy storage devices, the spectroscopically resolved behavior of single ions holds significant potential to elucidate the chemical processes occurring within a battery, from electrolyte to electrodes. This includes de-solvation, intercalation, and other critical mechanisms. By providing insights into specific phenomena like dendrite growth and solid-electrolyte interphase (SEI) formation,²⁴ we believe this approach will drive the development of advanced batteries with enhanced cyclability and higher capacity. Our results on organic and aqueous electrolytes enable the investigation of various battery systems, including both alkali metal and aqueous batteries. The combination of high sensitivity, selectivity, and real-time monitoring capabilities makes our method a potentially transformative tool for these diverse applications.

Main

Point defects in h-BN can be intentionally induced in pristine material through large-area irradiation with ions or neutrons, or by oxygen plasma etching, as described in the Methods section. Using the plasma etching treatment, these point defects are discernible on the surface of h-BN through atomic resolution scanning transmission electron microscopy (STEM). This is illustrated in Fig. 1a, using integrated differential phase contrast (iDPC) mode. The point defects in h-BN are optically active, as schematically shown in Fig. 1b. When lithium ions approach and bond with these defects, there is a measurable change in emission properties. By monitoring these changes, we can effectively visualize individual lithium ions at the point defects.

The plasma-treated h-BN was fabricated into a microfluidic cell for imaging as shown in Extended Data Fig. 1 (see Methods). At the initiation of the experiment, there is an excess of emitters, which may stem from impurities and unstable defects on the surface of h-BN. Upon sample illumination, the emitted light underwent a photobleaching process before reaching a steady state as shown in Extended Data Fig. 2. After photobleaching, the emitter count per flake (N) was stable for observation times greater than 150 seconds at a frame rate of 10 Hz.

This study examines three lithium-ion electrolytes: fluoroethylene carbonate (FEC), propylene carbonate (PC), and dimethyl sulfoxide (DMSO). Figures 1c-h depict the consecutive super-resolution localization images of emitters on the same flake in the steady state over 1500 frames in three electrolytes, both without (Fig. 1 c-e) and with (Fig. 1 f-h) Li^+ . The statistical summary of the emitter count per flake is depicted in Figures 1i-k. It is evident that the count (N) increases by more than fivefold in all three electrolytes. This increase

occurs alongside the presence of lithium ions in the electrolytes, and the distribution of N conforms to the Poisson distribution.

To investigate the underlying interaction between Li^+ and point defects in h-BN, we employed a multispectral localization approach to simultaneously image the position and spectral characteristics of the emitters (see Methods).²⁵ We presented the emission signals of single emitters on identical flakes, both with and without lithium ions in the electrolytes, along with their respective spectral information, as illustrated in Fig. 2a. Figure 2b shows the averaged spectra of all the emitters across identical flakes in electrolytes with and without lithium-ions. It is worth noting that the presence of lithium ions in the electrolytes leads to a red shift over 10 nm in wavelength, as depicted in Figure 2 through the spectra of single emitters (Fig. 2a) and averaged spectra from multiple emitters across a flake (Fig. 2b).

Through localizing the emitters, we can extract and analyze the spectra of the same defects across various electrolytes, as demonstrated in Extended Data Fig. 3. Clearly, a consistent red shift was observed in these spectra, suggesting the influence of the ionic environment on defective states. The distribution of the photoluminescence peak of the emitters used for averaging in Fig. 2b is shown in Extended Data Fig 4, where a similar red shift is observed. This shift could be attributed to the weak interactions between Li^+ and point defects, which will be discussed in detail in a later section.

To ascertain that the observed emission shift is due to Li^+ rather than anions or organic solvent molecules, we modified our experimental device for incorporating electrodes (see Methods). This allows us to apply an electric field to control the ion movement and distribution. Fig. 3a and 3b schematically illustrate this process: applying a positive voltage to the copper input electrode (V_{input}) relative to the indium tin oxide (ITO) creates an electrolyte double layer,²⁶ leading to the accumulation of lithium cations (Li^+) on the surface of the h-BN (Fig. 3a). Conversely, a negative voltage at the copper electrode repels lithium ions from the h-BN surface (Fig. 3b).

We began our experiments by applying a square wave voltage to the input electrode (V_{input}) with a cycle period of 30 seconds. The emitter counts per 100 msec frame, shown as red dots in Fig. 3c, rises and falls in sync with the square wave transitions. At -1 V, when anions accumulate on the surface of the h-BN, the emitter's counts are low. Conversely, at +1V, lithium ions accumulate on the surface, causing a significant increase in the emitter number.

Figures 3 d and e display the super-resolution reconstructed images of the emitters during the last ten seconds of three-square wave pulses. This indicates that the emission is primarily activated by lithium ions, rather than other components in the electrolyte. Furthermore, the output waveform of the emitter count (N) resembles a square wave output from a first-order RC low-pass filter. By fitting the observed curve with exponential functions defined by the equations

$$N = P(1 - e^{-((t-t_0)/\tau)}) + Q$$

for the rising phase and

$$N = P e^{-((t-t_0)/\tau)} + Q$$

for the falling phase, we can extract the steady-state counts of emitters at -1 V ($Q \equiv N(t \rightarrow \infty) \approx 15$) and +1 V ($P + Q \approx 63$), along with the time constant $\tau \approx 6$ s. This analysis yields a quantitative measure of the emitter dynamics under varying voltage conditions, details of which will be elaborated upon in subsequent sections.

Spectral analysis provides insights into the chemical behaviors and local ionic bonding configurations within materials. Figure 3f shows the spectra of emitters during the last ten seconds of each square wave pulse. At -1 V, the photoluminescence peak lies between 570 and 610 nm, indicating a weak interaction of h-BN flakes in DMSO with lithium ions, as shown in Fig. 2. In contrast, at +1 V, a significant red shift is observed, with the photoluminescence peak moving to ~ 650 nm. This shift suggests that chemical bonding changes occur between lithium ions and defects in h-BN, likely due to the de-solvation and subsequent insertion of lithium ions into these point defects.

Additionally, Extended Data Fig. 5 shows a marked increase in the current profile at +1 V, indicating substantial electrochemical reactions. To understand the red shift, density functional theory (DFT) calculations were performed to examine the local electronic band structure of h-BN. As depicted in Extended Data Fig. 6b, intrinsic h-BN exhibits a bandgap of about 4.55 eV, with the nitrogen p orbitals contributing to the valence band density of states (DOS) and the boron p orbitals to the conduction band DOS.

The analysis included boron vacancies (V_B), nitrogen vacancies (V_N), and boron-nitrogen pair vacancies (V_{BN}). Defect formation energies indicate that under boron-deficient conditions, V_B forms with lower energy (see Extended Data Fig. 6). When a lithium ion adsorbs onto the h-BN surface (Extended Data Fig. 7), the adsorption energy calculations show a stronger attachment at the boron vacancy, suggesting a higher reactivity of V_B towards lithium ions.

The Fig. 3i presented shows two calculated densities of states (DOS) for h-BN defects. The top panel illustrates the DOS for a bare h-BN defect (V_B^-), while the bottom panel displays the DOS for the h-BN defect with a lithium ion (V_B^-Li). The shaded region represents the intermediate state, corresponding to the defect level. The DOS for V_B^- reveals an intermediate energy level approximately 1.58 eV above the valence band, attributed to the unpaired electron in the nitrogen p orbital (Fig. 3g). While with lithium ion, the interaction between the lithium s orbital and the nitrogen p orbitals (Fig. 3h) shifts the intermediate level closer to the conduction band to ~ 1.02 eV. During the process of 532 nm laser excitation, electrons are excited above this intermediate state and then relax back to it. Subsequently, these electrons combine with holes in the valence band, emitting a fluorescence signal. The shift in the intermediate state, observed in the presence of the lithium ion, leads to a corresponding shift in the fluorescence spectrum, reflecting the change in the defect's electronic structure. The calculated spectrum shift based on the DOS is larger than experimental observations, which may be due to the exchange-correlation functional approximation effect or basis set limitation, but it qualitatively reflects the trend.

To further understand the dynamic behaviors, we applied a sinusoidal voltage waveform with an amplitude of 1V across two electrodes, varying the frequency from 0.02 Hz to 5 Hz (Fig. 4a). At lower frequencies, the emitter counts varied sinusoidally with the voltage waveform. As the frequency increased, the amplitude of these fluctuations decreased, becoming negligible above 1 Hz. Fourier analysis of the input voltage signal (V_{input}) and the resultant optical signal (N) showed that the electrolyte double layer acts as a low-pass filter. It amplifies signals at lower frequencies and attenuates those above a cutoff frequency near 1 Hz, where noise becomes dominant. This behavior matches the modeled equivalent circuit of the electrolyte double layer,²⁷ which includes a large double-layer capacitor and a solvent resistance (Extended Data Fig. 8).

Figure 4c displays the average spectra of all emitters at different frequencies during the V_{input} phase from $\pi/2$ to π (shadowed area in the inset). At 0.02 Hz, a dominant peak at ~ 650 nm aligns with results from a square wave at 1V, indicating complete formation of chemical bonds between lithium ions and h-BN defects. At 2 Hz, multiple peaks below 600 nm and between 600-650 nm suggest emissions from intrinsic defects, weak Coulombic interactions, and incomplete bonding between h-BN defects and Li^+ with solvation structure. The persistence of the 650 nm peak implies that some ions remain embedded within defects, unable to detach during the negative phase. Therefore, although the impedance measurement can respond to frequencies up to 100 kHz, the electrical signal is indeed due to ion migration. The actual electrochemical reactions require significantly longer time (less than 1 Hz, with a time constant of ~ 6 seconds).

Particularly, our approach can be expanded to visualize and differentiate diverse ions in various liquid environments. We started from imaging Li^+ , Zn^{2+} , and Al^{3+} in aqueous solution on an identical flake as shown by Fig. 5 a-c. The emitter count ratio in Li^+ , Zn^{2+} , and Al^{3+} solutions is 1:0.48:0.54. The emitter count exhibited varying activation capabilities for different ions. According to our findings, Li^+ ions exhibited strong activation, while the activation of Zn^+ and Al^{3+} ions was relatively weaker. This variation may arise from differences in ion size, hydration shell, and chemical affinity.

Subsequently, we simulated the presence of H^+ , Li^+ , Na^+ , K^+ , Zn^{2+} , Al^{3+} on different flakes in aqueous solutions to extract the spectral information, as shown in Fig. 5d. Our analysis categorizes the ions into three distinct groups. In terms of spectral peak positions (Fig. 5e), H^+ , Li^+ , and Na^+ exhibit centers ~ 575 nm, while K^+ and Zn^{2+} peak ~ 585 nm, and Al^{3+} at ~ 600 nm. A similar trend is observed in the full width at half maximum (FWHM), as shown in Fig. 5f.

Each ion presents a unique interaction profile. Additionally, the positioning and width of spectral peaks are correlated with the density of states and energy bands, which are intricately tied to the distribution of the electron cloud. For H^+ , Li^+ , and Na^+ ions, the outer electron orbitals correspond to 1s, 2s, and 3s, respectively. The hybridization between these s orbitals and nitrogen p orbitals is expected to produce similar spectral shifts due to their comparable electronic configurations and energy levels. This similarity in hybridization

among H^+ , Li^+ , and Na^+ ions result in analogous interaction patterns with the point defects in h-BN, leading to closely related spectral features.

In contrast, K^+ and Zn^{2+} possess 4s orbital in their outer electron shells. The higher principal quantum number and the spatial distribution of these 4s orbitals generate different hybridization with nitrogen p orbitals, leading to distinct interaction patterns and, consequently, unique spectral features. Furthermore, Al^{3+} , with its outer electron shell consisting of 2p orbitals, presents another hybridization scenario. The presence of p orbitals, as opposed to s orbitals, introduces additional complexity in the interaction with nitrogen p -orbitals, resulting in spectral features that differ from those observed with ions that have s orbitals as their outer shells. Therefore, the variations in electron orbital configurations and hybridization patterns among these ions — H^+ , Li^+ , Na^+ with 1-3 s orbitals, and K^+ , Zn^{2+} , Al^{3+} with higher-order or p orbitals—account for the differences in their spectral features when interacting with h-BN quantum defects.²⁸

These distinct spectral features enable the classification of ions in mixed solutions. In Fig. 5g, the h-BN flake was immersed in a solution containing a 1:1:1 ratio of Li^+ , Zn^{2+} , and Al^{3+} (1/3 M of each ion in deionized water). By monitoring the spectra of each emitter and measuring the Euclidean distance of each spectrum to the three standard spectra, the emitters can be classified into three groups: Li^+ (red), Zn^{2+} (blue), and Al^{3+} (yellow), as shown in Fig. 5g. Out of a total of 378 emitters, 172 interacted with Li^+ , 92 with Zn^{2+} , and 114 with Al^{3+} (1:0.54:0.66), indicating a classification based more on activation capabilities rather than the concentration ratio of these ions. The spectra displayed in Fig. 5h illustrate the integrated spectra of all emitters, with the respective contributions from Li^+ , Zn^{2+} , and Al^{3+} highlighted individually.

We note that we have not studied in detail transition metal ions with 3d orbital, such as Fe^{2+} , Fe^{3+} , Cu^{2+} , and Mn^{2+} . The divalent ions exhibit specific colors due to inter-orbital $d-d$ transitions and charge transfer transitions with the surrounding ligands (e.g., water molecules).^{29,30} This coloration could interfere with the emission caused by interactions with h-BN defects. In the case of Fe^{3+} with outmost electron configuration of $3s^2$, $3p^6$ and $3d^5$, we note that there no fluorescence in our optical detection window. While we have excluded a study of their fluorescence properties in this report, investigating these interactions in future studies would be valuable.

Conclusion

The advancements in this ion sensing platform, particularly through the spectral information, herald a new era of exploration at the single ion level within liquid environments. Capturing the spectral shifts of individual ions can offer important information about the dynamics of their interactions with surrounding environment in solution, and shed light on fundamental chemical processes of ion charge carriers with h-BN. In this study, we started from the Li^+ activation of the point defects in electrolytes, causing a spectral red shift of over 10 nm. Furthermore, we resolved electrochemical reactions in situ at the single-ion level via

applying an electrical field to manipulate the behaviors of Li^+ , evidenced by a significant spectral shift of around 50 nm. Combined with frequency domain analysis, we are able to separate the time constants of ion migration and electrochemical reactions. Finally, we extended this strategy to encompass multiple ions. The distinct spectral signatures of different ions, resulting from variations in their electronic structures, enable precise ion classification. This research platform to visualize and differentiate single ions in real-time provides opportunities for advancing our understanding of complex systems. In particular, we are applying this spectroscopy to explore innovative solutions to chemical energy storage, and other applications based on new materials.

Methods

Sample preparation:

Clean #1.5 glass coverslips served as the initial substrates, subjected to a sequential washing protocol involving acetone, isopropyl alcohol (IPA), a potassium hydroxide solution, and finally, deionized (DI) water. After cleaning, h-BN flakes were mechanically exfoliated from high quality crystals³¹ onto the substrate of coverslips. Surface activation was achieved through oxygen plasma etching performed with a March Instruments PX-250 Plasma Asher, employing a power setting of 75 W and an oxygen gas flow rate of 10 standard cubic centimeters per minute (sccm). Etching durations were 60 seconds for general sample preparation and increased to 120 seconds specifically for samples destined for electrical response analysis.

Samples allocated for electrical measurements were further processed by sputtering approximately 180 nm of indium tin oxide (ITO) onto the cleaned coverslips, followed by an annealing phase at 370 °C for one hour. After the mechanical exfoliation and plasma treatment, the construction of the counter electrode was carried out by affixing a polyimide (PI) Kapton film, upon which copper was sputtered, to the opposite side of the ITO-coated coverslip. This setup ensures the application of voltage for electrical measurements while preventing potential short circuits between the copper and ITO layers.

To construct the PDMS microfluidic channel, a mixture of polydimethylsiloxane (liquid) and a cross-linking agent is poured into a mold created from Kapton tape (~60 μm thick) and then heated to form an elastomeric replica. After the mold is cut and peeled away, a biopsy punch is used to create inlets and outlets for the electrolyte. The PDMS surface is subsequently treated with oxygen plasma and bonded to a glass coverslip. The electrolyte is introduced into the channel within an argon-filled glovebox and sealed with an additional PDMS layer on top. Lithium perchlorate (LiClO₄) was used as the lithium-ion source. A concentration of 1 M LiClO₄ was used for general imaging in Figs. 1 and 2, while a concentration of 0.1 M LiClO₄ was used for electrical response analysis in Figs. 3 and 4. For imaging multiple ions, sulfate salts were used, including Li₂SO₄, Na₂SO₄, K₂SO₄, ZnSO₄, and Al₂(SO₄)₃, each at a cation concentration of 1M in Milli-Q deionized water. The imaging of H⁺ was using the Milli-Q deionized water directly with a PH value of ~7.¹⁸

For the TEM imaging, the sample was initially exfoliated onto a PDMS substrate and then transferred to a microporous SiN_x TEM grid using a deterministic transfer method. Prior to the transfer, the SiN_x grid was sputtered with a ~5 nm thick Pd/Au alloy to facilitate charge dissipation during imaging.

Optical setup:

The microscopy setup utilized a 532 nm laser (Cobolt 06-DPL 532nm 200mW laser) for wide-field excitation via an oil immersion objective (Nikon CFI SR HP Apo TIRF 100XC Oil, NA: 1.49). Wide-field excitation was directed to the backplane of the sample with a power density of 4000 W/cm². After passing through a 200 mm infinity-corrected tube lens (Thorlabs, TTL200MP), the emission signal was collected through the same objective. The

signal underwent further refinement through a series of optical filters—including a dichroic beam splitter (Semrock, FF535-SDi01-25x36), a notch filter (Thorlabs, NF533-17), a long-pass filter (Thorlabs, FELH0550), and a short-pass filter (Thorlabs, FESH0800). It was then concentrated using a 300 mm achromatic doublets lens (Thorlabs, AC508-300-AB). After initial focusing, the luminescence was split by a nonpolarizing 50/50 beam splitter (Thorlabs, BSW10R) into positional and spectral channels. Each channel was focused by a 180 mm doublets lens (Thorlabs, AC508-180-AB) and recombined using a knife-edge mirror (Thorlabs, MRAK25-P01) onto the left and right halves of an EMCCD camera (iXon Ultra 897 EMCCD). To disperse the spectral signal, an equilateral prism (PS863, Thorlabs) was positioned at the Fourier plane of the final focusing lens. A series of narrow band-pass filters (Thorlabs, FBH570-10, FBH600-10, FBH650-10, FBH694-10, FBH750-10) and standard fluorescent nanodiamond nitrogen vacancy were used to calibrate the spectra before data collection. During imaging, the EM gain was set to 200, and the frame rate was adjusted to 10 Hz for samples destined for electrical response analysis. For imaging multiple ions in deionized water, the microscopy was set to total internal reflection fluorescence (TIRF) mode to reduce background signal, using a lower excitation power of 2000 W/cm².

Optical data processing:

Two background images were utilized to subtract the baseline from the raw data. The first, termed the absolute background, is an averaged image captured in an area devoid of h-BN samples but under identical excitation conditions. Additionally, a reference background specific to each emitter was employed when extracting spectral information. This reference background comprises the average image of ten neighboring frames that do not contain the emitter of interests. The emitter count and super-resolution reconstruction were carried out using the ImageJ plugin, ThunderSTORM.²⁰ For spectrum extraction, emitters located on the edges, those overlapping (required to be at least 50 pixels apart to prevent spectral overlap), and those with insufficiently low intensities were excluded from the analysis.

TEM:

The STEM images were acquired on Thermo Fisher Spectra 300 monochromated, double-corrected scanning transmission electron microscope. The high voltage is 300 kV and the convergence semi-angle is 30 mrad with sub-angstrom probe. IDPC-STEM images³² are acquired under ~ 10 pA beam current by using four-segmented DF-S detectors. The camera length is 185 mm. IDPC images are processed by using Velox software. The acquired image was digitally processed through a bandpass filter to highlight the lattice spots.

Theoretical computation:

We conducted spin-polarized density functional theory (DFT) calculations using the Vienna ab initio Simulation Package (VASP-5.4.4)³³ within the python-based Atomic Simulation Environment (ASE).³⁴ The Perdew-Burke-Ernzerhof (PBE)³⁵ functional within the generalized gradient approximation (GGA) described the exchange and correlation interactions. The projector-augmented plane wave (PAW) method with a kinetic energy cut-off of 600 eV was used to treat ion-electron interactions, ensuring well-converged results. The k-point mesh

was sampled using the Monkhorst-Pack scheme. To correct for van der Waals interactions, the DFT-D3 method with Becke-Johnson damping was employed.

Our calculations utilized a (5×5) four-layer h-BN surface containing 200 atoms, derived from an optimized bulk structure. For bulk calculations, a primitive unit cell and a 7×7×3 k-point grid were used for geometry optimization. In surface calculations, a 20 Å vacuum was applied between repeating slabs to prevent spurious image-charge interactions. The bottom two layers were fixed to the bulk geometry, while the top two layers and adsorbates (Li-ion) were allowed to relax during surface geometry optimization, below a force threshold of 0.01 eV/Å. A 3×3×1 k-point grid was used for surface geometry optimization, and a higher k-point grid for density of states (DOS) calculations.

The methodology for defect formation energy and Li-adsorption energy was adopted from previous works.³⁶ For visualization and analysis of the crystal structure, we used the ASE visualization suite and VESTA software.

Acknowledgement

We thank Prof. Harold Y. Hwang for the discussion. The optical experiments are supported by the Laboratory Directed Research and Development program at SLAC National Accelerator Laboratory, under contract DE-AC02-76SF00515. The device fabrication was supported by U.S. Department of Energy (DOE), Office of Basic Energy Sciences, Division of Materials Sciences and Engineering under contract DE-AC02-76SF00515. Yecun Wu and Yi Cui acknowledge the partial support from U.S. Department of Energy (DOE), Office of Basic Energy Sciences, Division of Materials Sciences and Engineering under contract DE-AC02-76SF00515. Yan-Kai Tzeng acknowledges the support from U.S. Department of Energy of the Battery500 Consortium program. Work was performed in part in the nano@Stanford labs including Stanford Nano Shared Facilities (SNSF) and Stanford Nanofabrication Facility (SNF), which are supported by the National Science Foundation as part of the National Nanotechnology Coordinated Infrastructure under award ECCS-2026822.

Author contributions

Y.W., Y.-K.T., and S.C. designed the research; Y.W. performed device fabrication, optical measurement, and data analysis; K.X. performed TEM measurement under supervision of A.M. H.P.S. performed theoretical computation under supervision of F.A.P.; T.T. and K.W. supplied the h-BN crystals; Y.C. discussed and assisted in analyzing the data; Y.W., Y.-K.T., S.C. wrote the manuscript with comments from all the authors.

References

1. Miller, C. Ion channel structure and function. *Science* **258**, 240–241 (1992).
2. Anastassopoulou, J. & Theophanides, T. The Role of Metal Ions in Biological Systems and Medicine. *Bioinorg. Chem.* 209–218 (1995).
3. Malik, L. A., Bashir, A., Qureashi, A. & Pandith, A. H. Detection and removal of heavy metal ions: a review. *Environ. Chem. Lett.* **17**, 1495–1521 (2019).
4. Liu, C. *et al.* Lithium Extraction from Seawater through Pulsed Electrochemical Intercalation. *Joule* **4**, 1459–1469 (2020).
5. Fritz, J. S. Ion Chromatography. *Anal. Chem.* **59**, 335–344 (1987).
6. Kanu, A. B., Dwivedi, P., Tam, M., Matz, L. & Hill, H. H. Ion mobility–mass spectrometry. *J. Mass Spectrom.* **43**, 1–22 (2008).
7. Lockyer, N. P. *et al.* Secondary ion mass spectrometry. *Nat. Rev. Methods Prim.* **4**, 1–21 (2024).
8. Deslignière, E. *et al.* Ultralong transients enhance sensitivity and resolution in Orbitrap-based single-ion mass spectrometry. *Nat. Methods* **2024** *214* **21**, 619–622 (2024).
9. Gumpu, M. B., Sethuraman, S., Krishnan, U. M. & Rayappan, J. B. B. A review on detection of heavy metal ions in water – An electrochemical approach. *Sensors Actuators B Chem.* **213**, 515–533 (2015).
10. Cui, L., Wu, J. & Ju, H. Electrochemical sensing of heavy metal ions with inorganic, organic and bio-materials. *Biosens. Bioelectron.* **63**, 276–286 (2015).
11. Ghittorelli, M. *et al.* High-sensitivity ion detection at low voltages with current-driven organic electrochemical transistors. *Nat. Commun.* **2018** *91* **9**, 1441 (2018).
12. Quang, D. T. & Kim, J. S. Fluoro- and chromogenic chemodosimeters for heavy metal ion detection in solution and biospecimens. *Chem. Rev.* **110**, 6280–6301 (2010).
13. Wu, D. *et al.* Fluorescent chemosensors: the past, present and future. *Chem. Soc. Rev.* **46**, 7105–7123 (2017).
14. Aharonovich, I. & Toth, M. Quantum emitters in two dimensions. *Science* **358**, 170–171 (2017).
15. Gottscholl, A. *et al.* Initialization and read-out of intrinsic spin defects in a van der Waals crystal at room temperature. *Nat. Mater.* **19**, 540–545 (2020).
16. Tran, T. T., Bray, K., Ford, M. J., Toth, M. & Aharonovich, I. Quantum emission from hexagonal boron nitride monolayers. *Nat. Nanotechnol.* **2015** *111* **11**, 37–41 (2015).
17. Grosso, G. *et al.* Tunable and high-purity room temperature single-photon emission from atomic defects in hexagonal boron nitride. *Nat. Commun.* **2017** *81* **8**, 1–8 (2017).
18. Comtet, J. *et al.* Direct observation of water-mediated single-proton transport between hBN surface defects. *Nat. Nanotechnol.* **2020** *157* **15**, 598–604 (2020).
19. Ronceray, N. *et al.* Liquid-activated quantum emission from pristine hexagonal boron nitride for nanofluidic sensing. *Nat. Mater.* **22**, 1236–1242 (2023).
20. Ovesný, M., Křížek, P., Borkovec, J., Švindrych, Z. & Hagen, G. M. ThunderSTORM: a comprehensive ImageJ plug-in for PALM and STORM data analysis and super-resolution imaging. *Bioinformatics* **30**, 2389–2390 (2014).
21. Lelek, M. *et al.* Single-molecule localization microscopy. *Nat. Rev. Methods Prim.*

- 2021 11 1, 1–27 (2021).
22. Betzig, E. *et al.* Super-resolved Fluorescence Microscopy: Nobel Prize in Chemistry 2014 for Eric Betzig, Stefan Hell, and William E. Moerner. *Angew. Chemie Int. Ed.* **53**, 13972–13977 (2014).
 23. Moerner, W. E. & Fromm, D. P. Methods of single-molecule fluorescence spectroscopy and microscopy. *Rev. Sci. Instrum.* **74**, 3597–3619 (2003).
 24. Larcher, D. & Tarascon, J. M. Towards greener and more sustainable batteries for electrical energy storage. *Nat. Chem.* 2014 71 **7**, 19–29 (2014).
 25. Moon, S. *et al.* Spectrally Resolved, Functional Super-Resolution Microscopy Reveals Nanoscale Compositional Heterogeneity in Live-Cell Membranes. *J. Am. Chem. Soc.* **139**, 10944–10947 (2017).
 26. Wu, Y., Li, D., Wu, C. L., Hwang, H. Y. & Cui, Y. Electrostatic gating and intercalation in 2D materials. *Nat. Rev. Mater.* **8**, 41–53 (2023).
 27. Jossen, A. Fundamentals of battery dynamics. *J. Power Sources* **154**, 530–538 (2006).
 28. Wang, L. C., Zhang, Z. C., Ma, L. C., Ma, L. & Zhang, J. M. First-principles study of hydrogen storage on Li, Na and K-decorated defective boron nitride nanosheets. *Eur. Phys. J. B* 2022 953 **95**, 1–14 (2022).
 29. Holmes, O. G. & McClure, D. S. Optical Spectra of Hydrated Ions of the Transition Metals. *J. Chem. Phys.* **26**, 1686–1694 (1957).
 30. Crosby, G. A. Spectroscopic Investigations of Excited States of Transition-Metal Complexes. *Acc. Chem. Res.* **8**, 231–238 (1975).
 31. Taniguchi, T. & Watanabe, K. Synthesis of high-purity boron nitride single crystals under high pressure by using Ba-BN solvent. *J. Cryst. Growth* **303**, 525–529 (2007).
 32. Lazić, I., Bosch, E. G. T. & Lazar, S. Phase contrast STEM for thin samples: Integrated differential phase contrast. *Ultramicroscopy* **160**, 265–280 (2016).
 33. Kresse, G. & Furthmüller, J. Efficient iterative schemes for *ab initio* total-energy calculations using a plane-wave basis set. *Phys. Rev. B* **54**, 11169 (1996).
 34. Hjorth Larsen, A. *et al.* The atomic simulation environment—a Python library for working with atoms. *J. Phys. Condens. Matter* **29**, 273002 (2017).
 35. Blöchl, P. E. Projector augmented-wave method. *Phys. Rev. B* **50**, 17953 (1994).
 36. Sarker, H. P., Rao, P. M. & Huda, M. N. Niobium Doping in BiVO₄: Interplay Between Effective Mass, Stability, and Pressure. *ChemPhysChem* **20**, 773–784 (2019).

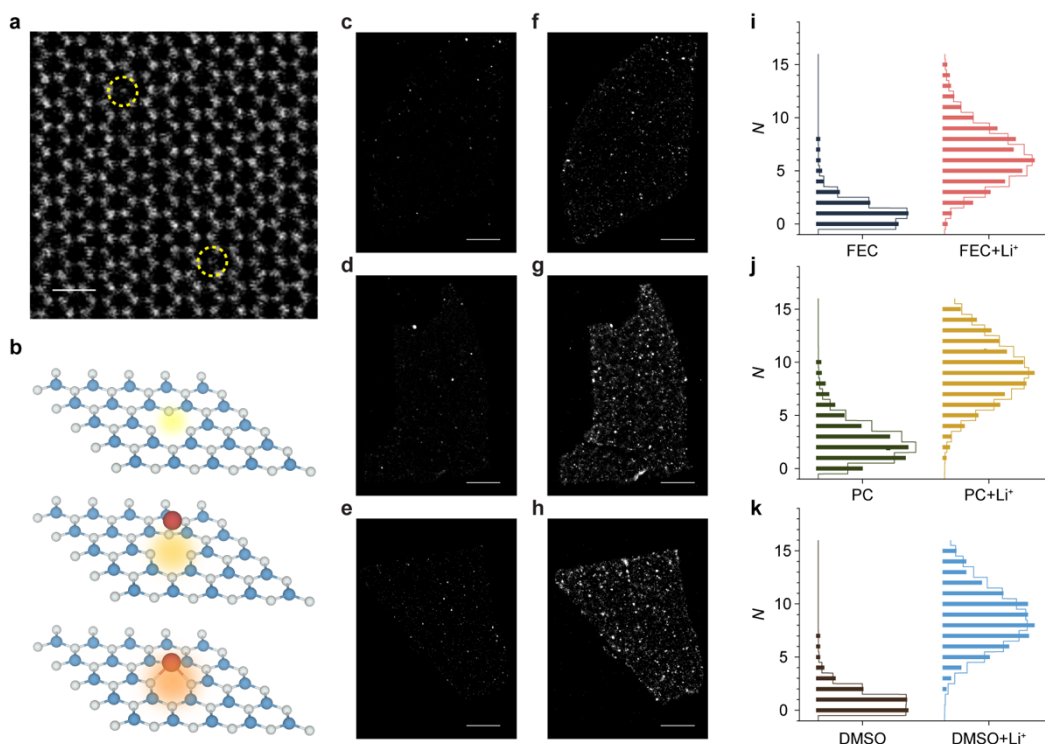


Fig. 1: Visualization of Li^+ activation of quantum defects in h-BN.

a, Integrated differential phase contrast (IDPC)-scan transmission electron microscopy (STEM) image of an oxygen plasma treated few-layer h-BN (scale bar: 500 nm). The yellow dashed circles indicate point defect in h-BN. **b**, Schematic representation of the configuration of an h-BN defect and a Li^+ , showing three scenarios: an intrinsic defect, a defect with a nearby Li^+ , and a defect bonded with Li^+ . **c-e**, Super-resolution images of h-BN flakes in various electrolytes: pure FEC (**c**), PC (**d**), and DMSO (**e**), reconstructed from a sequence of 1500 frames in steady-state (from 1001 to 2500 frame). **f-h**, Comparative super-resolution images of the identical h-BN flakes in FEC (**f**), PC (**g**), and DMSO (**h**) electrolytes supplemented with 1M LiClO_4 , generated from 1500 frames in steady-state. Scale bar: 3 μm . **i-k**, Statistical distribution of the number of emitters (N) per frame from the sequence of 1500 frames in panels **c-h**, in different electrolytes, both without and with 1M LiClO_4 . The curves are fitted with Poisson distribution.

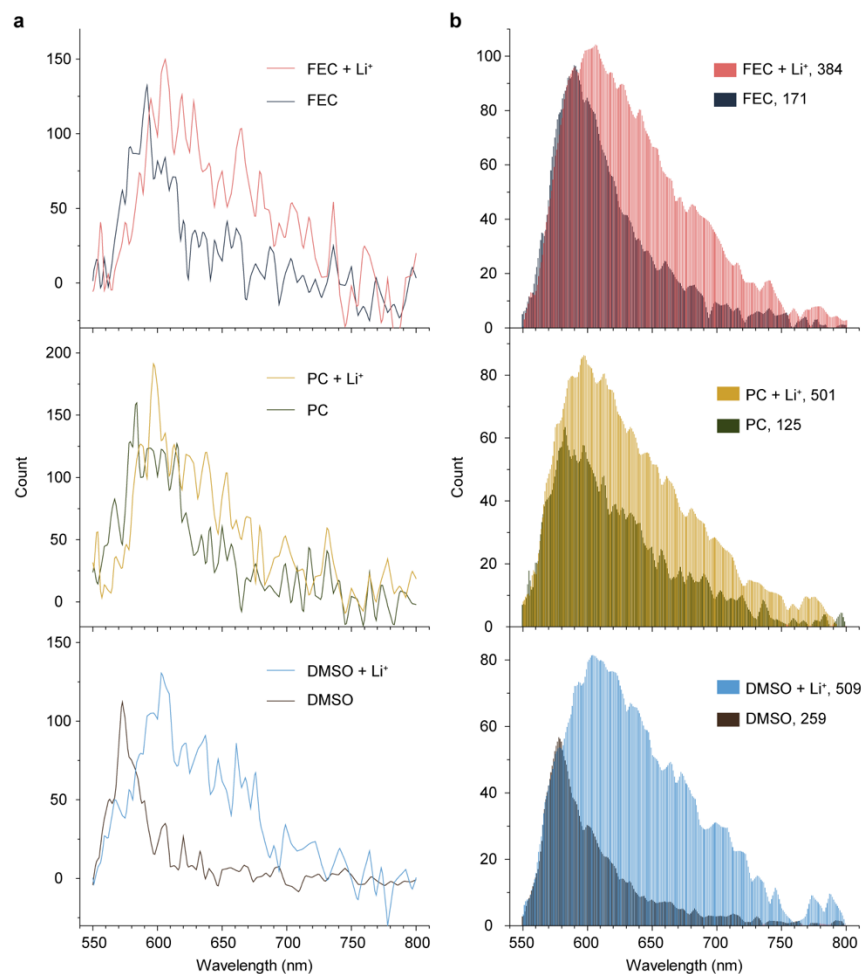


Fig. 2: Emitter spectra within different electrolytic environments with and without Li⁺.

a, Emission spectra from single quantum emitters in various electrolytes, differentiated by the presence of Li⁺. The presented spectra are averaged from over four frames featuring the same emitter. **b**, Composite spectra consolidating the average emissions from all emitters on a single h-BN flake, compiled from over 1000 frames. Legends denote the type of electrolyte and the count of emitters analyzed for the average.

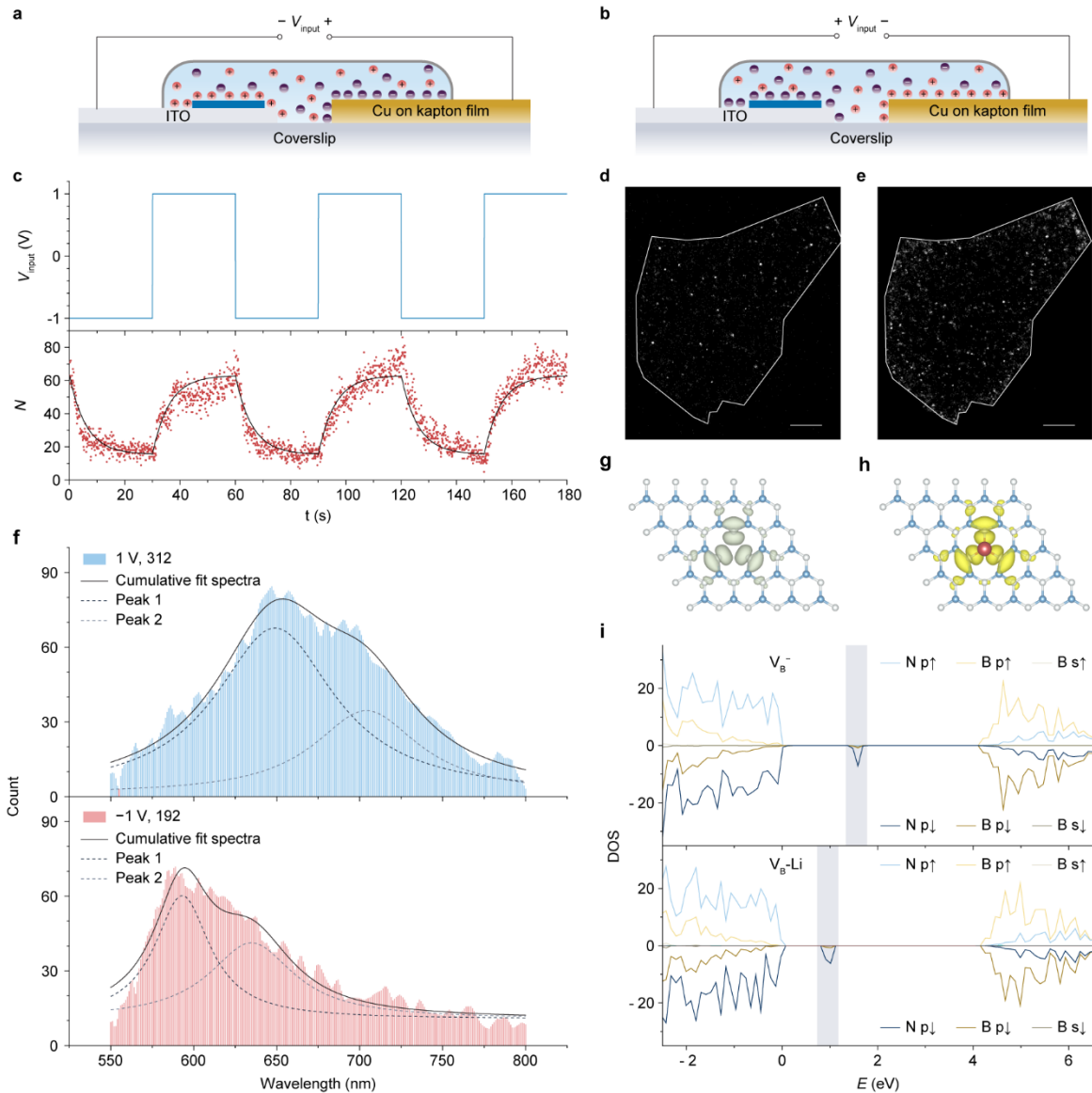


Fig. 3: Spectra indicated electrochemical reactions on the surface of h-BN.

a-b, Schematic illustration of the cell setup and ion distribution under varying voltages. With a positive V_{input} (**a**), Li^+ are drawn towards the h-BN surface, creating an electrolyte double layer. Conversely, when a negative V_{input} (**b**) is applied, anions accumulate on the h-BN surface. **c**, Voltage profile of the V_{input} square wave (top, blue) contrasted with the resultant emitter count fluctuations per frame (bottom, red). The black line in the bottom graph represents the output fitting to a standard RC low-pass filter, modeling the system's response. **d** and **e**, Super-resolution images of the h-BN flake captured at -1 V (**d**) and +1 V (**e**), reconstructed from data collected in the last 10 seconds prior to the voltage switch, specifically at intervals of 20-30s, 80-90s, and 140-150s for -1 V, and 50-60s, 110-120s, and 170-180s for +1 V. Scale bar: 2 μm . **f**, Combined emission spectra from all emitters on a single h-BN flake, recorded under varying applied voltages and sourced from the frames utilized for the reconstructions in panels **d** and **e**. The dashed lines represent the fitted peaks,

while the solid lines represent the cumulative fitted spectra. **g** and **h**, Calculated electron contributions of V_B^- h-BN and Li^+ at the V_B . **i**, DOS of the V_B^- h-BN and Li^+ bonds with the V_B .

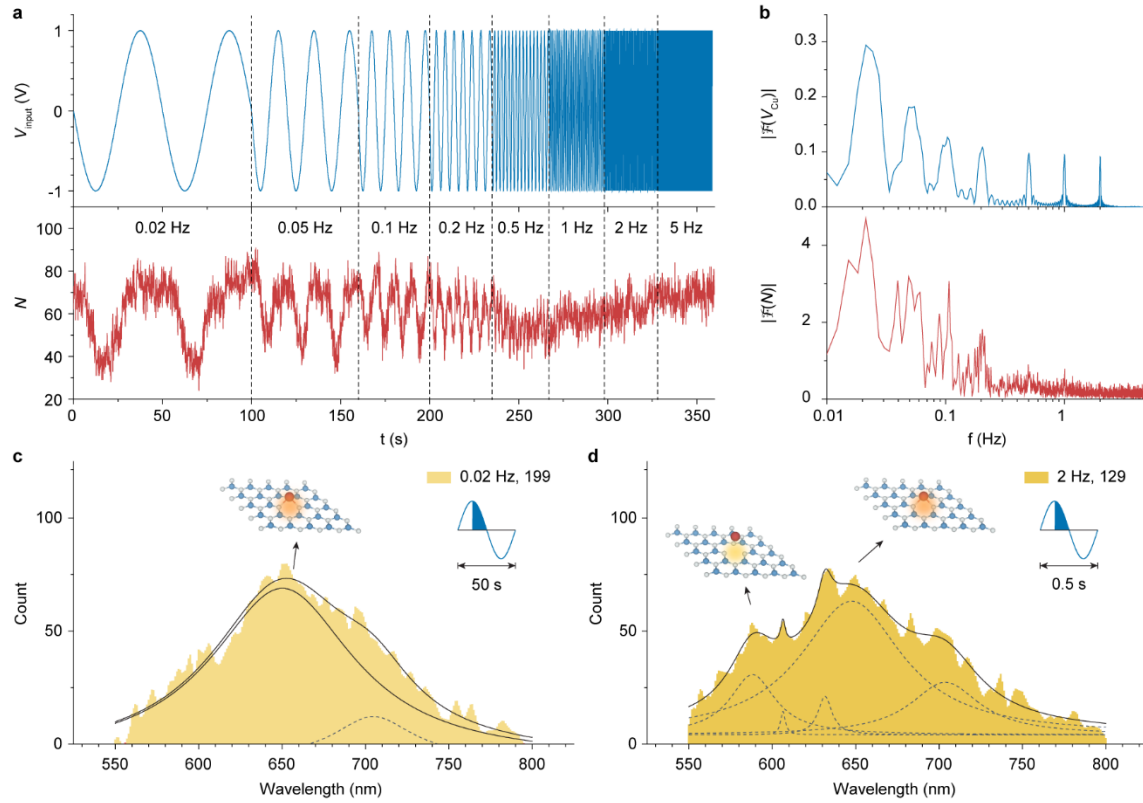


Fig. 4: Frequency domain analysis of ion dynamics under electrical field.

a, Voltage profile of the applied sine wave at different frequencies to the Cu electrode and the respective variation in quantum emitter count per frame. **b**, Fourier transform amplitudes for the applied voltage (input signal) and the optical emitter count (output response) across varying frequencies. **c** and **d**, Averaged spectra obtained from the emitters during the V_{input} phase from $\pi/2$ to π (as indicated by the shadowed area in the inset) at 0.02 Hz (**c**) and 2 Hz (**d**). The numbers following the legend represent the count of emitters used to average the spectra. The dashed lines represent fitted peaks using Lorentzian fitting, while the solid lines represent the cumulative fitted spectra. The inserted schematic illustrations depict the configurations of a boron vacancy with Li^+ and their corresponding emissions.

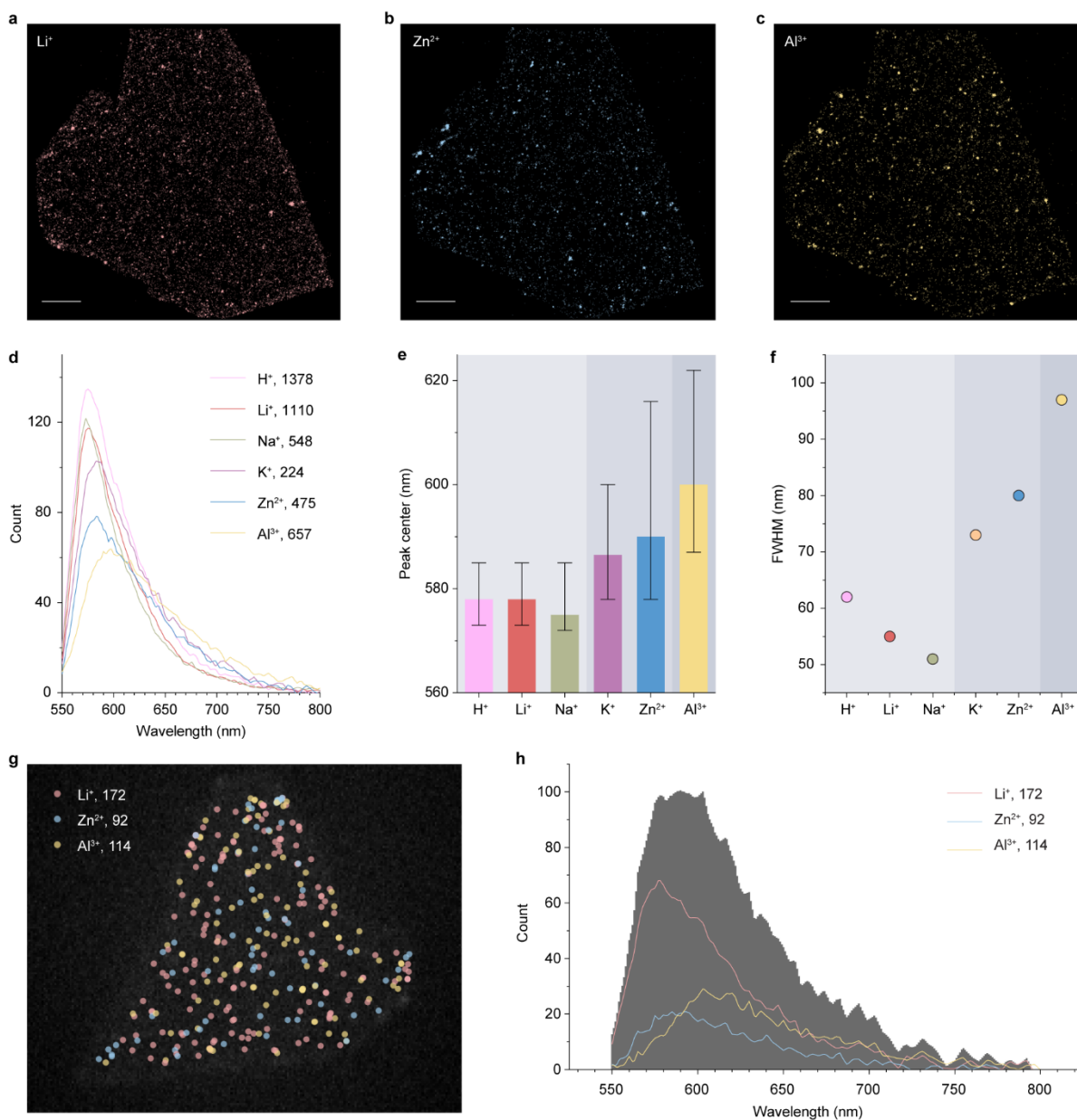
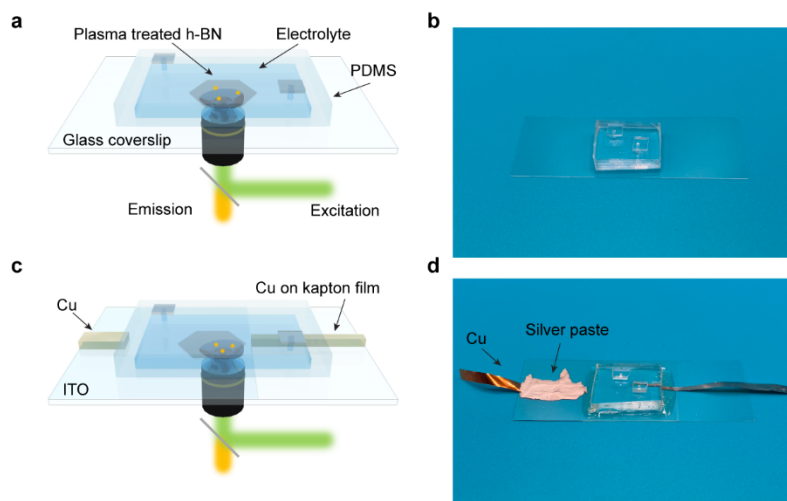


Fig. 5: Differentiation of multiple ions.

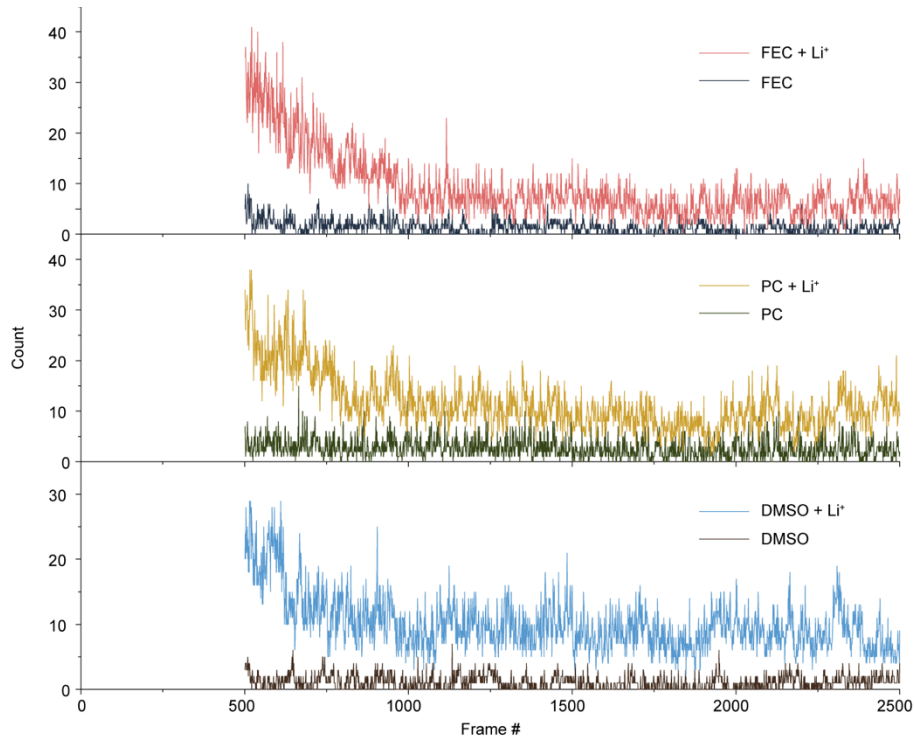
a-c, Reconstructed super-resolution image of the same flake in aqueous solutions with H^+ (**a**), Li^+ (**b**), and Na^+ (**c**). Scale bar: 2 μm . **d**, Spectra of h-BN flakes in aqueous solutions with different ions, with the numbers in the legend indicating the count of emitters used to average the spectra. **e**, Positions of peak center for the spectra in different solutions. The error bars represent the interquartile range (25% – 75%) of the peak center distribution. **f**, Variation of full width at half maximum for the spectra in different solutions. **g**, Classification of multiple ions in an aqueous solution. Out of 378 emitters, 172 interacted with Li^+ , 92 interacted with Zn^{2+} , and 114 interacted with Al^{3+} . **h**, Averaged integrated spectra (shadow area) of all 378 emitters in panel **g**, with colored lines representing the integrated spectra of different ions across the total number of emitters.



Extended Data Fig. 1: The schematic and photographs of the cell.

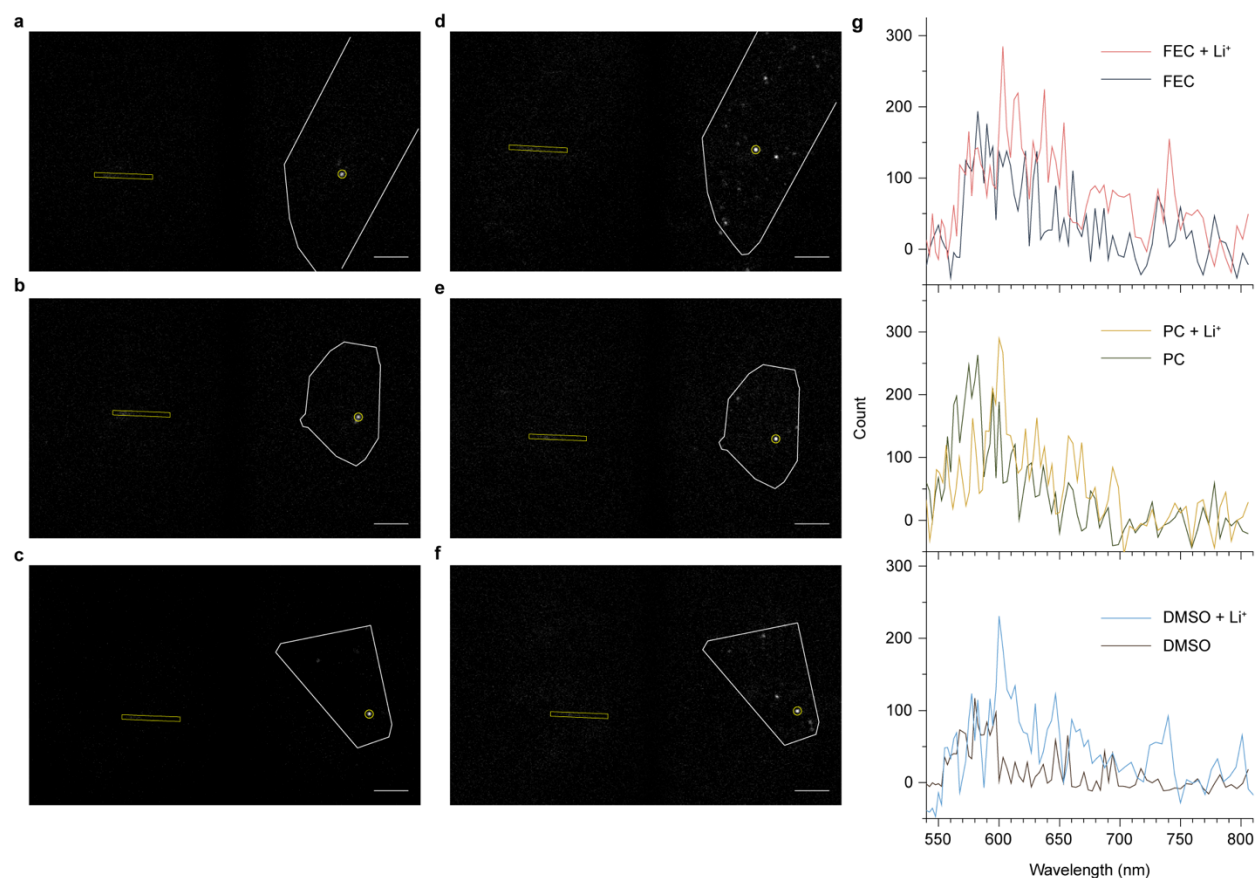
a-b, Schematic illustration (**a**) and photograph (**b**) of a standard imaging microfluidic device.

c-d, Schematic illustration (**c**) and photograph (**d**) of a microfluidic device equipped with electrodes for electrical testing.



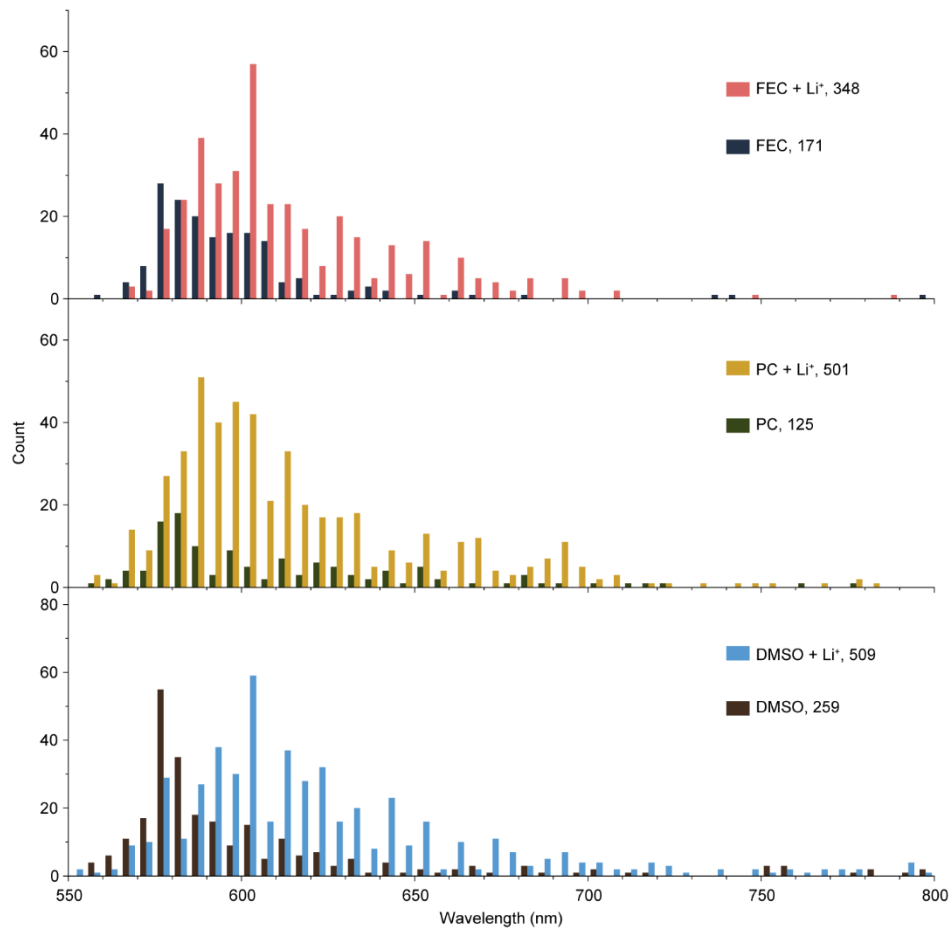
Extended Data Fig. 2: The count of emitters as a function of illumination time for the identical flakes in electrolytes with and without lithium ions.

The counts stabilize at a steady state after 1000 frames in different electrolytes, both with and without lithium. Before reaching 500 frames, the high density of emitters combined with the manual focus process makes it impossible to accurately count the number.

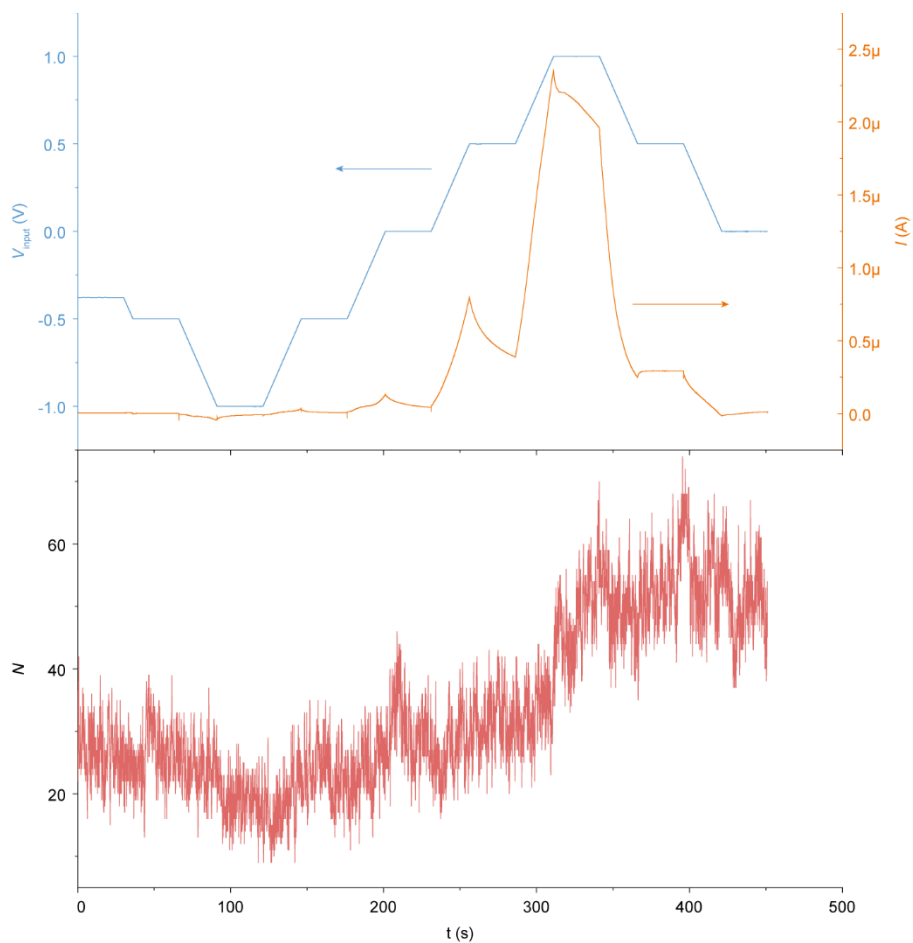


Extended Data Fig. 3: The spectra of emitters located on the same flake and in the same spot within an electrolyte, with and without lithium ions.

a-f, Sample field of view (after background subtraction) showing positional information (left half) and spectral information (right half) for each emitter (scale bar: 40 μm) in pure FEC (**a**), PC (**b**), DMSO (**c**), 1M LiClO₄ in FEC (**d**), 1M LiClO₄ in PC (**e**), and 1M LiClO₄ in DMSO (**f**) electrolytes. The white lines delineate the edges of the flakes, and the yellow frame indicates the corresponding spectral range. **g**, the extracted spectra from the yellow frames in panel **a-f**.

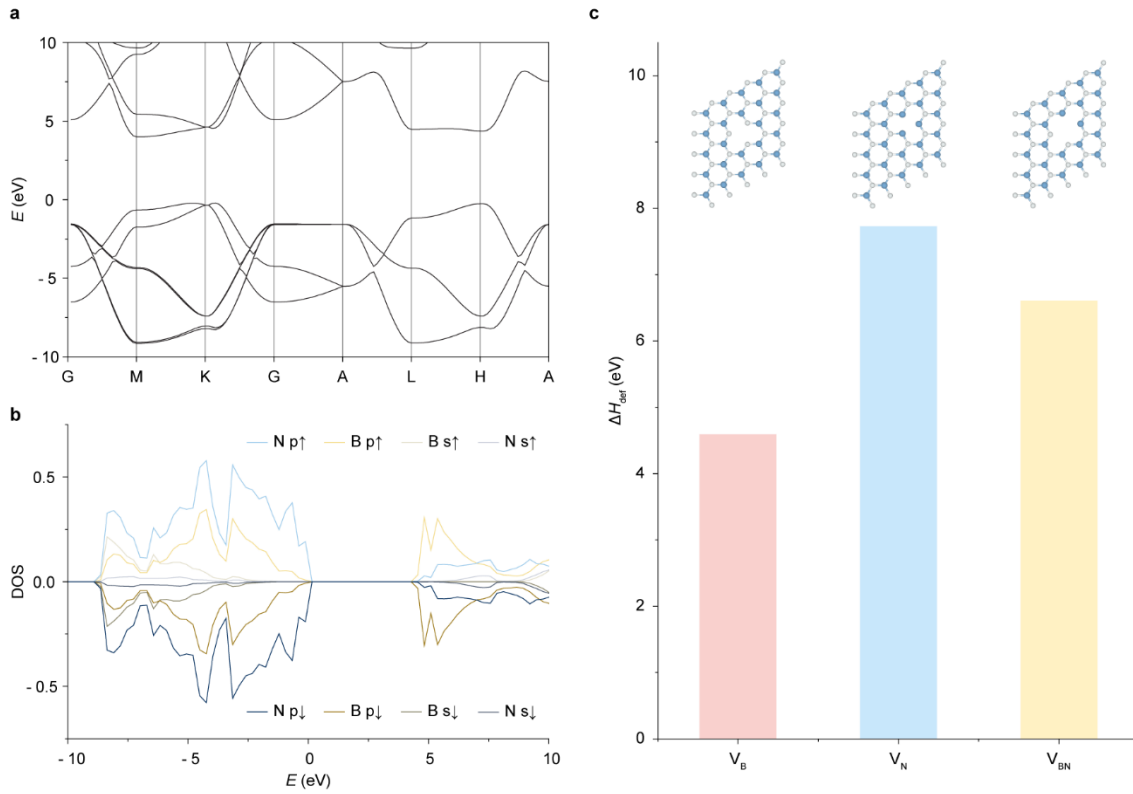


Extended Data Fig. 4: The distributions of the peak centers of emitter spectra in various pure electrolytes and electrolytes with 1M LiClO₄. The spectra are extracted from the same flake for identical solvents. The numbers following the legend labels indicate the total number of emitters for each distribution.



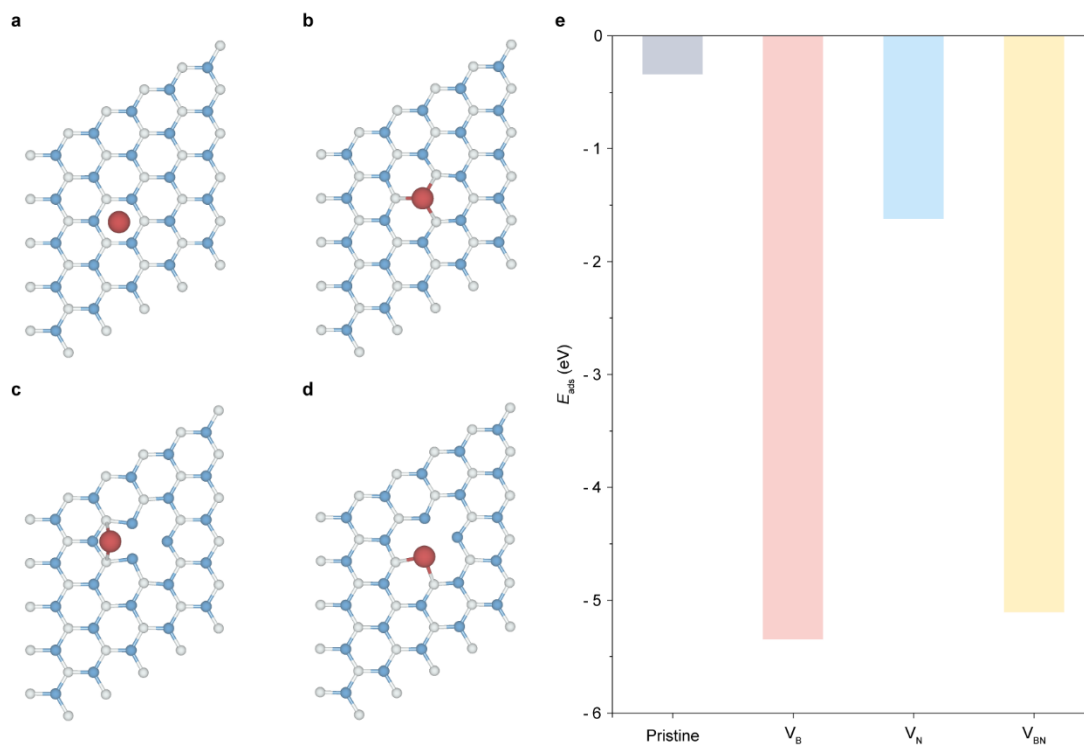
Extended Data Fig. 5: The voltage-current profile and count of emitters per frame as a function of time.

The V_{input} (up, blue) is scanned from the open circuit voltage to -1 V, then forward to 1 V, and finally back to 0 V. The scan rate is 20 mV/s, and the voltage is held for 30 seconds at each 0.5 V step. The higher current (up, orange) observed when the voltage is positive suggests electrochemical reactions. The count of emitters (bottom, red) varies with the voltage with a hysteresis.

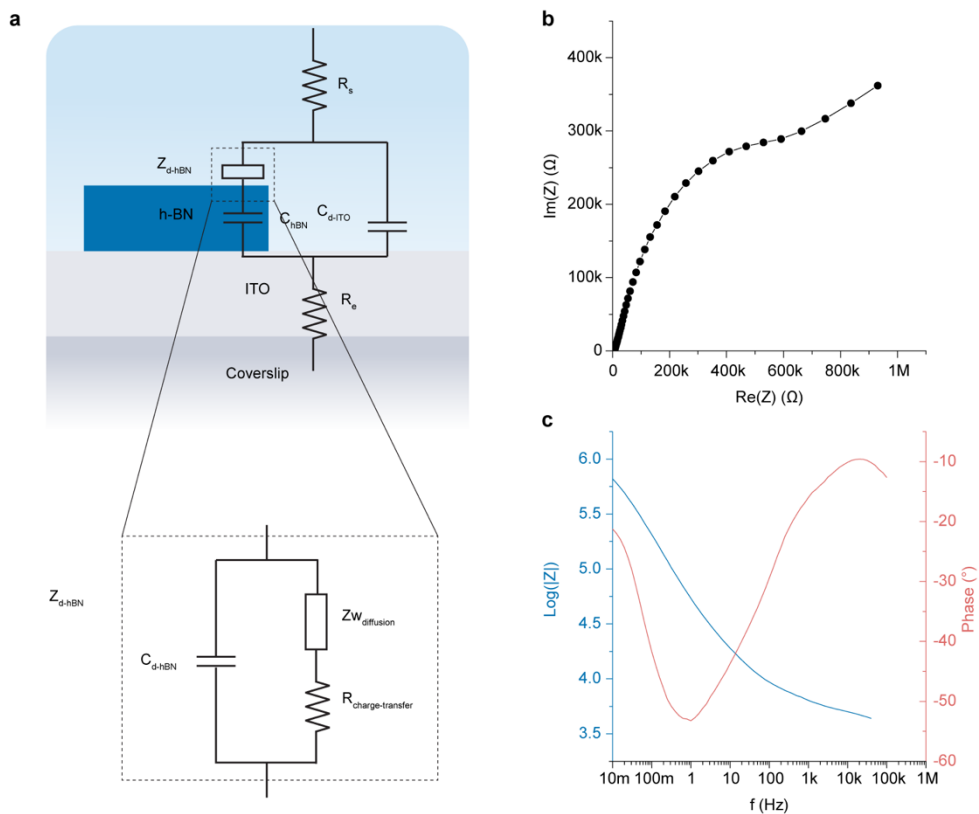


Extended Data Fig. 6: Theoretical model and calculation.

a, The electronic band structure of intrinsic h-BN. **b**, The spin-resolved DOS of the intrinsic h-BN. **c**, Calculated defect formation energy (ΔH_{def}) for various types of defects, with insets showing schematic illustrations of the defect configurations.



Extended Data Fig. 7: Lithium adsorption energy on different configurations of defects. **a-d**, Schematic representations of lithium ion adsorption on h-BN with different configurations: pristine, V_B , V_N , and V_{BN} . **e**, Comparative graph of the Li^+ adsorption energy (E_{ads}) across these defect configurations.



Extended Data Fig. 8: The equivalent circuit and impedance measurement of the cell.

a, The equivalent circuit. The impedance of the double layer formed on the surface of h-BN (Z_{d-hBN}) consists of a double-layer capacitor (C_{d-hBN}) in parallel with a diffusion impedance, which is in series with a charge-transfer resistance due to electrochemical reactions on the surface. **b** and **c**, The Nyquist (**b**) and Bode (**c**) plot of the impedance measurement of the whole cell.